

Helium-W co-deposition layer: TEM observation and D retention

Shin Kajita*

Institute of Materials and Systems for Sustainability, Nagoya University, Nagoya 464-8603, Japan

Kosuke Asai and Noriyasu Ohno, Hirohiko Tanaka

Graduate School of Engineering, Nagoya University, Nagoya 464-8603, Japan

Naoaki Yoshida

RIAM, Kyushu University, 6-1 Kasugakoen, Kasuga-shi, Fukuoka 816-8580, Japan

Daisuke Nagata, Miyuki Yajima

National Institute for Fusion Science, Oroshi-cho, Toki, Gifu 509-5292, Japan

(Dated: June 23, 2020)

Co-deposition of wall material and ions from plasmas occurs on material surfaces in fusion devices. In this study, we focus on tungsten (W) deposition layer in helium (He) plasmas (He-W co-deposition) formed at surface temperatures of 473-773 K. Usually, He irradiation at the surface temperature below 1000 K does not lead significant morphology changes; we will show from transmission electron microscope observations that the roughness of the co-deposition layer has a significant temperature dependence even when the temperature is less than 800 K. We conducted deuterium plasma irradiation to the He-W co-deposition layer. It was found that the deuterium retention on the He-W co-deposition layer increased significantly with increasing the formation temperature of the co-deposition layer.

I. INTRODUCTION

Tungsten (W) is one of the leading candidates of plasma facing components in fusion devices. They are subjected to ions of mainly hydrogen isotopes (D and T) and the nuclear reaction product of helium (He) in fusion devices. The behaviors of D/T and He are quite different; exposures to hydrogen isotopes leads to blisters [1, 2], while exposures to He causes various morphology changes accompanied by He bubble growth [3]. The most significant one is likely to be the growth of fiberform nanostructures (fuzz) [4].

Concerning the fuzz growth, because of its importance in fusion devices, the formation condition [5, 6], mechanism, and influence on the fusion reactor including enhanced erosion [7], dust formation, and initiation of arcing [8] have been discussed. Also, the growth rate has been well investigated including the fluence and temperature dependence [6, 9, 10], the effects of annealing [11–13], sputtering [14–16], and transients [17, 18]. A growth model including pulses of edge localized modes (ELMs) has been developed by De Temmerman *et al.* [19, 20]. It was shown that the fuzz layer thickness strongly depended on the ELM heat load and the base temperature, and the thickness would be $\sim 1.5 \mu\text{m}$ when the base temperature was 1200 K and the ELM heat load was less than 0.2 MJm^{-2} assuming that the ELM frequency was 30 Hz.

However, we think that there are still several not well-known factors for the He irradiation effects. Recently,

under RF conditions [21] or with a small amount of impurity (argon, neon, or nitrogen) [22], isolated structures called nano-tendrils bundles (NTBs) were found. Sputtering from the surface was suggested to be important for the NTB growth [23]. Moreover, when supplemental W source was added near a W substrate during He plasma exposure, mm-thick large-scale fiberform nanostructures (LFNs) were grown [24, 25]. In fusion devices, small amount of impurity is used as a radiator, and sputtering and re-deposition occur especially during ELMs [26]. Thus, investigation of He irradiation effects with under environments with redeposition are of importance.

Until now, several investigations about co-deposition layer using magnetron sputtering devices have been reported, and effects on the morphology changes and deuterium (D) retention have been discussed. Helium plasma irradiation has been conducted to a deposition layer formed under He and argon mixture plasmas [27]. Protrusions were found after the He plasma irradiation at 1500 K even though the He fluence ($3.6 \times 10^{23} \text{ m}^{-2}$) was an order of magnitude lower than the incubation fluence for the fuzz growth [9]. Tang *et al.* formed co-deposition layers in a mixed atmosphere of D, He, and argon (Ar) [28]; they have found that amount of retained He had significant impact on the surface morphology, crystal structure, and D retention. De Temmerman and Doerner fabricated W co-deposition layers under D and Ar mixture conditions [29]. Many blisters were formed when the D fraction increased, and they discussed the relation between the D retention and the incident ion energy / surface temperature.

In this study, we formed W deposition layers in He plasmas at surface temperatures lower than the fuzz growth temperature of ≈ 1000 K. The temperature range

* kajita.shin@nagoya-u.jp

used in this study was lower than the one previously investigated for the growth of LFNs [24]. The He flux was in the range of $2.8\text{-}6.9 \times 10^{21} \text{ m}^{-2}\text{s}^{-1}$, which was much greater than those in magnetron sputtering devices. In addition to detailed observation using transmission electron microscope (TEM), the co-deposition layer was exposed to deuterium plasmas and retention was investigated using thermal desorption spectroscopy (TDS).

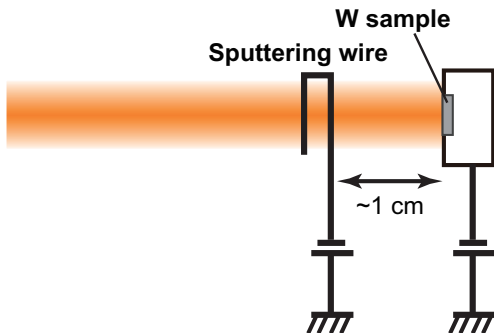


FIG. 1. A schematic of the experimental setup of the He plasma irradiation in the Co-NAGDIS device.

II. METHODS

A. Irradiation experiments

Figure 1 shows a schematic of the experimental setup of the He plasma irradiation with W deposition. Helium plasma irradiation was conducted in the linear plasma device Co-NAGDIS [30], where steady state plasmas with the density of the order of 10^{18} m^{-3} can be produced by a direct current arc discharge. The background pressure was $\approx 10^{-4} \text{ Pa}$, and the gas pressure was in the range of 2.0-2.8 Pa. Two serpent shaped lantern hexaboride are heated by a Joule heating and used for the cathode. A 0.1 or 0.2-mm-thick W sheet was installed to an air-cooled sample holder, which has a thermocouple to measure the sample temperature, T_s . The sample is polycrystal W (Plansee, 99.97%) without being recrystallized. Surface was polished to a mirror finish, and, then, an ultrasonic cleaning was performed. The temperature gradient cannot be formed in the codeposition layer even if the thermal conductivity is lower than the bulk in steady state conditions, though the pulse response can be altered depending on the pulse width [31]. Also, the temperature difference between the top and rear surfaces is negligible under steady state conditions, because the sample is thin. The temperature can be controlled by changing the air flow of the holder. The ion flux to the sample was measured from the current to the sample, and the incident ion energy, E_i , was measured from the potential difference between the potential of the sample, which was biased negatively, and the space potential deduced from a reciprocating electrostatic probe near the target.

A 1-mm-diameter W wire, which is referred to as sputtering wire in this study, was installed approximately 10 mm from the sample. The sputtering wire was biased negatively to -300 V to initiate sputtering. Thus, the sample was subjected to W particles in addition to He ions. The ionization mean free path of W atoms from the sputtering wire can be calculated using a typical density of $1 \times 10^{18} \text{ m}^{-3}$, the ionization rate coefficient of $8 \times 10^{-13} \text{ m}^3/\text{s}$ at 5 eV [32], and the mean energy of sputtered atom (5.8 eV) at the incident ion energy of 300 eV [33]. The mean free path is calculated to be $\approx 3 \text{ mm}$, which is shorter than the distance to the substrate; most of the sputtered atoms should be ionized before reaching the sample surface.

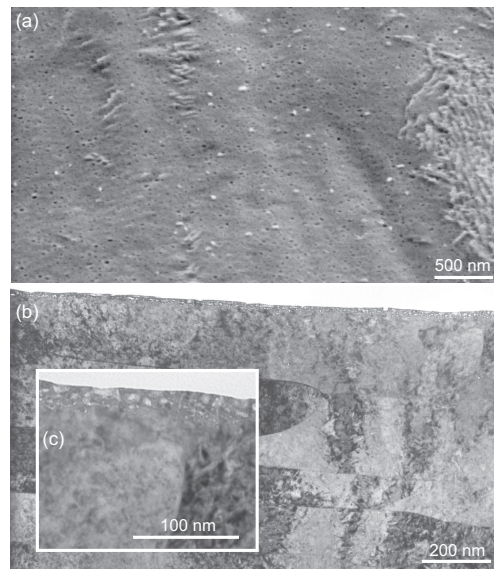


FIG. 2. (a) An SEM micrograph and (b,c) cross sectional TEM micrographs of W3 sample, which is W deposition layer at 773 K exposed to the He plasma.

B. Samples

Table I shows the details of the samples used in this study. Six co-deposition samples, He-W1–6, were prepared at three different temperatures, i.e. 471/473, 573, and 773 K, using W sheets for substrates. The irradiation time, t_i , was 3600 s, and E_i was in the range of 61-63 eV, and the He ion fluence, Φ_{He} , was in the range of $1.0\text{-}2.5 \times 10^{25} \text{ m}^{-2}$. Pairs of odd and even numbered samples (He-W1 and He-W2, He-W3 and He-W4, and He-W5 and He-W6) had almost identical He plasma irradiation condition. The odd numbered He-W samples were used for TEM observation, and the samples with even numbers were exposed to D plasmas after the He plasma exposure and analyzed with TDS. We optimized the spectrum width of high resolution quadrupole mass spectrometer for TDS and confirmed that there was no overlap between the D_2 and He spectra at the peak posi-

tions, where we used the values for desorption data. The both values were calibrated using tracer gas leak standards. The thicknesses of the deposition layer on He-W1, He-W3, and He-W5 measured from the TEM cross sectional images were 100, 200, and 460 nm, respectively. The thickness of the sample should be caused from the differences in the particle (W) flux to the sample if the porosity of the deposition layer was the same. The thickness of He-W5 was greater than that of He-W3, mainly because of the difference in the He flux, i.e. the density of the plasma. Another factor is the configuration of the sputtering wire to the target. We should admit that a slight difference in the position could have been influenced the thickness of the layer and sometimes formed non-uniformity.

In addition to the co-deposition samples, three more samples (W1-W3) were prepared for comparison; W1 was a W sheet sample exposed to D plasma without He plasma irradiation, and W2 was a W sheet sample exposed to the He plasma at 773 K and followed by D plasma irradiation. Concerning W3, W deposition layer was formed on a W sheet using a magnetron sputtering device while a substrate was heated at 773 K in Ar gas atmosphere (1 Pa); the thickness of the thin film was ≈ 180 nm. The sample (W3) was exposed to the He plasma and D plasma. The irradiation condition of the deuterium plasma irradiation was the same for all the samples (He-W2, He-W4, He-W6, W1, W2, and W3) and as follows: $E_i=62$ eV, $\Phi_D=8.7 \times 10^{24}$ m $^{-2}$, $t_i=3600$ s, and $T_s=373$ K. TEM samples were fabricated by focused ion beam (FIB) milling; typically, the thickness of the sample was 100 nm or less. Following two protective layers were put on the surface before the FIB cut process: 1- μ m-thick carbon deposition layer and 3-5- μ m-thick W deposition layer over the carbon layer.

III. MORPHOLOGY OF CO-DEPOSITION LAYERS

A. W deposition at 773 K

Before showing He-W co-deposition layers, here we show He plasma irradiation effects on W deposition layer (W3 sample) for a reference. Again, the thin film was deposited using a magnetron sputtering device with Ar gas environment at 773 K. Then, the sample was exposed to the He plasma in the Co-NAGDIS device under the condition shown in Table I.

Figure 2(a) shows an SEM micrograph of W3 sample. Many pinholes, the size of which was typically 10 nm, are found on all over the surface. Moreover, small protrusions and terrace structures can be seen on some locations. These are typical He irradiation effects observed in the initial formation process of nanostructures [34]. Figure 2(b,c) shows cross sectional TEM micrographs of W3 sample in different magnifications. The boundary of the thin film and substrate can be hardly discerned. There

is a thin layer near the surface (typically 50-nm-thick), where many He bubbles are identified. On the contrary, no damages are found below the layer. The size of bubbles is from several to 20 nm; the shape of the bubble is not round but distorted.

B. He-W Co-deposition layer

Figure 3(a,b) shows TEM micrographs of He-W1 sample in various magnifications. The co-deposition layer, which has a thickness of 90 nm, has a quite different feature from the bulk; there are nanometer sized voids and bubbles all over the layer. Below the co-deposition layer, He bubbles with several nanometers in diameter can be found; the thickness of the bubble existing layer below the co-deposition layer is approximately 20 nm. Those bubbles were likely formed in the initial irradiation process before the co-deposition layer was grown.

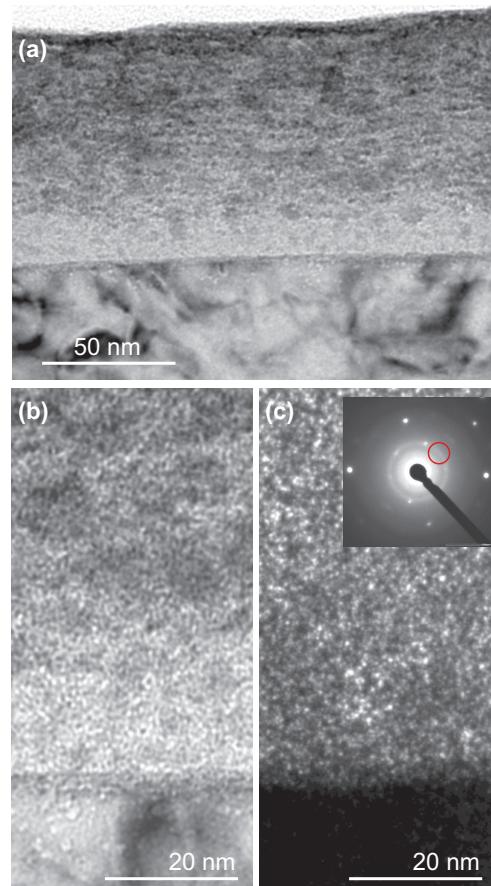


FIG. 3. (a,b) TEM micrographs of He-W1 sample (He-W co-deposition formed at 471 K) in different magnifications and (c) DFI image of He-W1 sample.

Figure 3(c) shows a dark field imaging (DFI) image of He-W1 sample. In the inset, diffraction pattern is shown, and a part of the diffraction ring shown with a red circle was chosen to obtain Fig. 3(c). The diffraction ring is

TABLE I. Experimental conditions for the preparation of the samples used in this study. Condition of the deuterium plasma irradiation was the same for all the samples and as follows: $E_i=62$ eV, $\Phi_D=8.7\times 10^{24}$ m $^{-2}$, $t_i=3600$ s, and $T_s=373$ K.

Name	Substrate	V_{sw} [V]	E_i [eV]	T_s [K]	Φ_{He} [m $^{-2}$]	t_i [s]	Thickness [nm]	D irradi.	Analysis
He-W1	W sheet	-300	62	471	1.0×10^{25}	3600	100	–	TEM
He-W2	W sheet	-300	62	473	1.0×10^{25}	3600	–	○	TDS
He-W3	W sheet	-300	61	573	1.1×10^{25}	3600	200	–	TEM
He-W4	W sheet	-300	62	573	1.0×10^{25}	3600	–	○	TDS
He-W5	W sheet	-300	63	773	2.5×10^{25}	3600	460	–	TEM
He-W6	W sheet	-300	63	773	2.5×10^{25}	3600	–	○	TDS
W1	W sheet	–	–	–	–	–	–	○	TDS
W2	W sheet	–	63	773	2.5×10^{25}	3600	–	○	TDS
W3	Deposition	–	63	773	2.5×10^{25}	3600	–	○	TEM/TDS

rather broad, indicating that the size of the crystal grains is very small. Indeed, from the DFI image, the size of the grain is found to be several nanometers.

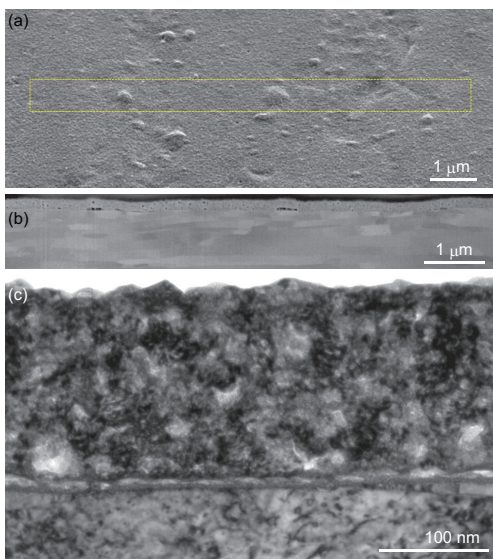


FIG. 4. SEM micrographs of He-W3 sample from (a) top and (b) side (cross section) and (c) a cross sectional TEM image of He-W3 sample.

Figure 4(a,b) shows SEM micrographs of He-W3 sample from top and side (cross section), respectively. The co-deposition layer was formed at T_s of 573 K, which is ≈ 100 K higher than that of He-W1 sample. From the cross-section image, it is found that many He bubbles exist in the co-deposition layer, which has the thickness of 190 nm. Blisters are found on the surface, and exfoliation of the deposition layer from the bulk are seen at some locations in the boundary beneath the blisters. The results suggested that the boundary between the bulk and the co-deposition layer was weak and diffused He could easily accumulate there. Figure 4(c) shows a cross sectional TEM image of He-W3 sample. The size of crystal grain is several tens of nanometers, which is greater than that of He-W1 sample. The boundary of the bulk and the co-deposition layer is clearly identified. It seems that there are elongated bubbles above the bulk. The results

suggest that the boundary can be a diffusion barrier; He atoms migrated were difficult to go to deeper region and accumulate on the boundary.

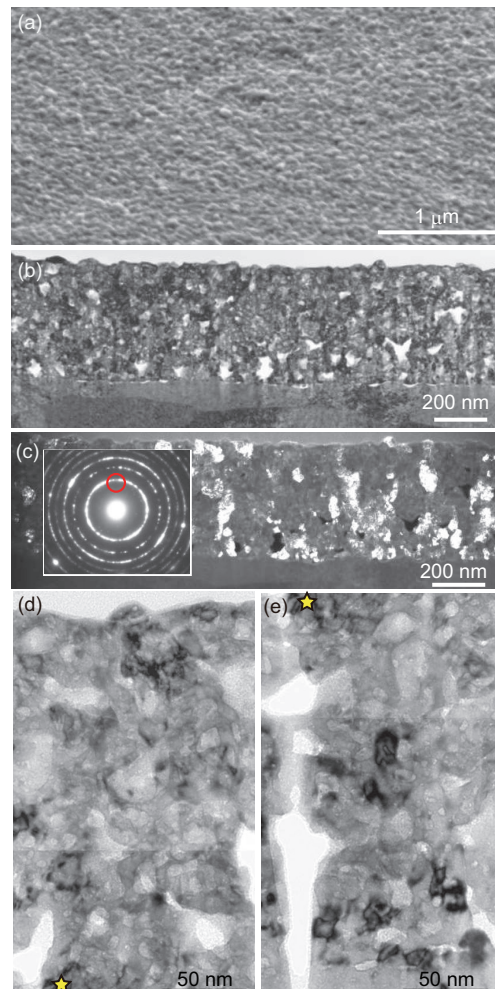


FIG. 5. (a) An SEM microscope of He-W5 sample, where the co-deposition layer was formed at 773 K, and cross sectional TEM (b) BFI image, (c) DFI image, and (d,e) BFI image in a larger magnification.

Figure 5(a) shows an SEM microscope of He-W5 sample, where the co-deposition layer was formed at 773 K.

The surface has a bumpy structure, the scale of which is ≈ 100 nm. Figure 5(b,c) shows cross sectional TEM bright field imaging (BFI) image and DFI image of He-W5 sample, respectively. The co-deposition layer, which has a thickness of ≈ 450 nm, is comprised of ≈ 100 -nm-sized microcrystals and voids. We can identify large sized voids near the boundary of the bulk material. Figure 5(d,e) shows cross sectional TEM micrographs in a larger magnification. The star marks in Fig. 5(d,e) corresponds to the same location of the sample. Vertically elongated voids are identified in Fig. 5(e); they could be formed during the FIB milling. It is seen that there are many He bubbles (less than several tens of nanometers) inside the microcrystals.

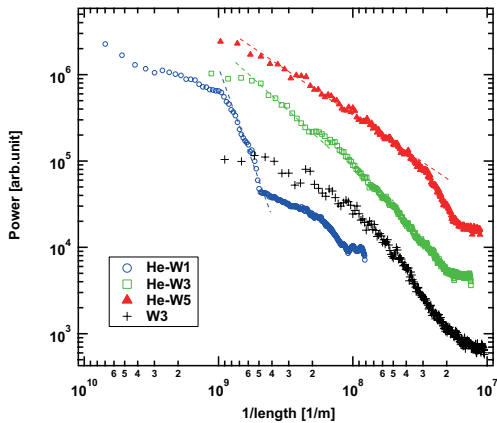


FIG. 6. FFT power spectra of W3, He-W1, He-W3, and He-W5. The FFT analysis was applied to the contrast variations of TEM images in horizontal direction.

To characterize the scale of He induced damages, fast Fourier transform (FFT) analysis was applied to the TEM micrographs. The contrast variation in horizontal direction is used for the analysis. Figure 6 shows power spectra of W3, He-W1, He-W3, and He-W5. On W3, the region where no apparent He-induced damages were identified was chosen; no clear peak is found, and the power spectrum gradually decreases with the inverse of characteristic length. The spectrum of He-W1 has a quite different feature. There is a steep slope from $5 \times 10^8 - 10^9 \text{ m}^{-1}$, which corresponds to 1-2 nm. This indicates that typical size of bubbles and crystal grain are less than 1-2 nm. Although it is less clear compared to He-W1, there is a similar slope in $2-5 \times 10^8 \text{ m}^{-1}$ on He-W3. No sharp slope is found on He-W5; a power law relation is identified in the FFT spectrum in the range less than $3 \times 10^7 \text{ m}^{-1}$ on He-W5. This could be because the He bubbles have fractality in the number-size relation, as was discussed previously on He irradiated metals (W and tantalum) [35, 36].

Energy-dispersive X-ray spectroscopy (EDS) analysis was conducted for He-W1, He-W3, and He-W5 samples. Figure 7(a-c) shows pairs of a TEM micrograph and a depth profile of normalized W signal intensity to that at the bulk for the three samples, respectively. The W den-

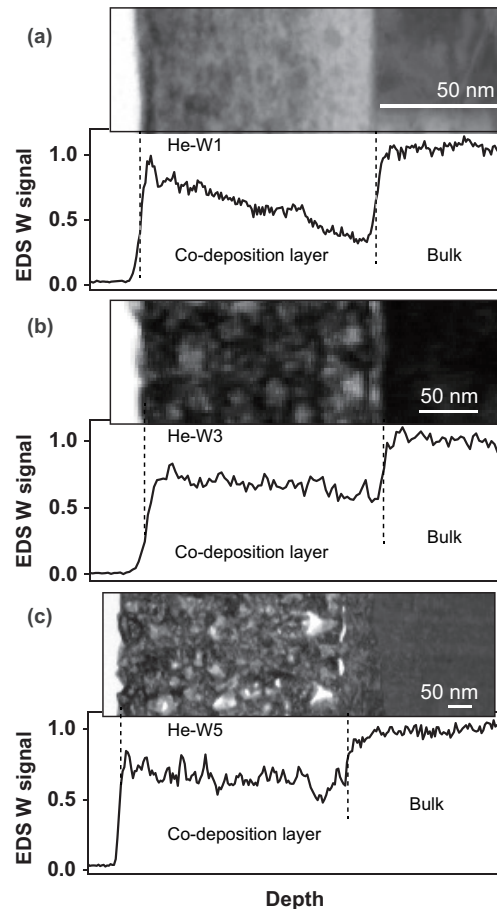


FIG. 7. Pairs of a TEM micrograph and a depth profile of normalized EDS W signal intensity to that at the bulk for (a) He-W1, (b) He-W3, and (c) He-W5.

sity gradually decreases on the co-deposition layer with the depth. In particular, it decreases significantly on He-W1 sample from 0.9 to 0.4 inside the co-deposition layer. A slight decrease with depth is identified on He-W3 sample, and a density dip, which was caused by pores above the bulk, is found on He-W5 sample. The decrease in the density with the depth suggested that He density increased with the depth. It is likely that there is a He diffusion barrier between the bulk and co-deposition layer, and diffused He atoms accumulate above the bulk layer, as was also identified in TEM micrographs. Assuming that the bulk was not influenced by the He plasma irradiation, the relative densities of the co-deposition layer estimated from the averaged EDS W signal intensity are 60.9 ± 14.3 , 67.9 ± 5.8 , and $65.6 \pm 6.6\%$ for He-W1, He-W3, and He-W5 samples, respectively; the difference was in the margin of error.

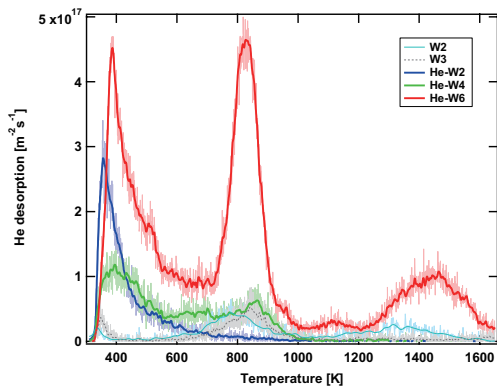


FIG. 8. He desorption rate as a function of the temperature from W2, W3, He-W2, He-W4, and He-W6. The ramping rate of the temperature was 0.5 K/s.

IV. ANNEALING EXPERIMENTS

A. He desorption and TEM observation

Figure 8 shows He desorption rate as a function of the temperature from W2, W3, He-W2, He-W4, and He-W6. The ramping rate of the temperature was 0.5 K/s. From W2 and W3 samples, after small peak at 350 K, another peak appears around 800 K; a small wide peak exists around 1300 K on W2. The He desorption from He-W co-deposition samples is quite different from those. The peak temperatures are similar, i.e., below 400 K and around 800 K, but the amount of desorption is much greater than those from W2 and W3. From He-W2 sample, one peak appears below 400 K, and the desorption continues to at ~ 700 K. The peak from He-W4 becomes broader and the desorption continues up to 900 K. When it comes to He-W6, three peaks are identified at ~ 400 , 800 and 1400 K, and the desorption is much greater than those at lower temperatures, i.e., He-W2 and He-W4.

Figure 9(a) and (b-i) shows TEM micrographs of cross section of He-W5 sample before and after annealing, respectively. The annealing was conducted for three minutes before taking images at (b) 600, (c) 700, (d) 800, (e) 900, (f) 1000, (g) 1100, (h) 1200, and (i) 1273 K in Fig. 9. It is noted that there are significant TDS desorption of He below 600 K, in the range of 700-900 K, and above 1200 K, as shown in Fig. 8. We call these peak A, B, and C, i.e., peak A (< 600 K), peak B (700-900 K), and peak C (> 1200 K) in this study. In this magnification, no significant changes are identified below the annealing temperature of 1100 K. At 1200 and 1273 K, shown in Fig. 9(g,h), the size of voids apparently increases. Figure 10(a-i) shows TEM micrographs in a larger magnification; the difference becomes notable in this magnification. Before annealing (Fig. 10(a)), there are many He bubbles in various scales. Comparing between Fig. 9(a) and (b), there are no significant changes. Thus, He desorption at peak A likely correspond to des-

orption from weak trapping sites such as distorted lattice in the vicinity of He bubbles, as was discussed previously for W exposed to He plasmas [37].

Around peak B (700-900 K), small bubbles less than 10 nm near the surface disappeared. Below 700 K, dislocations and distortion, which were presented as black lines, gradually decrease with increasing the temperature above 800 K. At 1200 K, which corresponds to peak C, a large void was formed in the bottom region of the TEM image. Almost all the distortion, presented as black lines, were diminished in this temperature range. Even at 1273 K, He bubbles less than 20 nm in diameter existed. In this temperature range, we have to bear in mind the fact that He atoms can be released from the side surfaces of the sample, because the thickness of the TEM sample was thinner than that of the deposition layer. Therefore, in real situations, He bubble growth would occur more significantly compared with the thin sample cases shown in Fig. 10.

B. D retention

Figure 11(a,b) shows D desorption rate from six samples: W1, W2, and W3 in Fig. 11(a) and He-W2, He-W4, and He-W6 in 11(b). On W1, which was not exposed to the He plasma, the desorption starts around 400 K and continued to 800 K. However, from W2 and W3, strong desorption peaks are identified just after increasing the temperature around 350 K with much greater desorption rate, while the desorption is terminated at a lower temperature of ~ 500 K. The results suggested that D atoms were trapped more weakly on W2 and W3 samples compared to W1. In addition, it was suggested that the D atoms only existed near the surface on W2 and W3, while D atoms were diffused to deeper region on W1. Concerning co-deposition samples (He-W2, He-W4, and He-W6), there is also a peak below 400 K with higher desorption peak than that of W1. In particular, on He-W6 sample, the desorption is much greater than those from the other sample. There was no significant D desorption above 700-800 K on all the samples. Thus, it can be said that D can be released from all the samples including the ones with a co-deposition layer when the temperature is higher than 700-800 K.

Figure 11(b) shows D total retention on the six samples; W1 had the lowest D retention and was $1.4 \times 10^{19} \text{ m}^{-2}$. The retention increased by 70% to $2.5 \times 10^{19} \text{ m}^{-2}$ on W2 sample, and the thin deposited layer sample (W3) was higher retention than that of bulk material (W2). Concerning the co-deposition samples, the retention increased with the temperature; He-W6 had $4.9 \times 10^{20} \text{ m}^{-2}$, which was more than 30 times greater than that of W1 and ten times greater than the He irradiated thin deposited layer sample (W3). Comparing between He-W4 and HeW6, even considering the fact that the deposition layer on He-W6 was roughly twice thicker than that of He-W4, the D retention per volume in the deposition

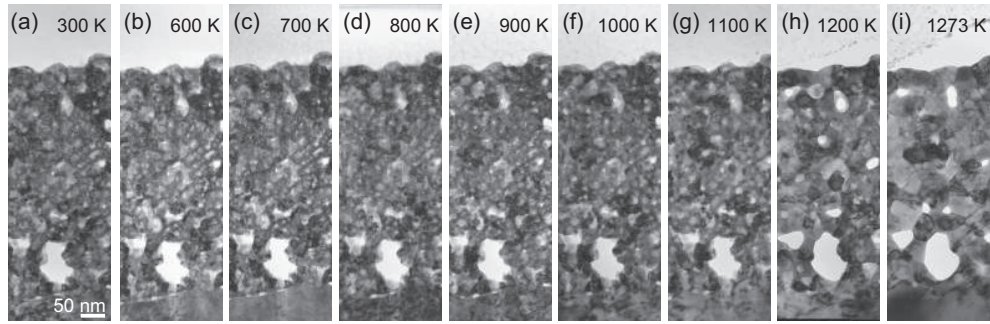


FIG. 9. TEM micrographs of cross section of He-W5 sample (a) before and (b-i) after annealing. The images were taken after annealing for three minutes at the temperature of (b) 600, (c) 700, (d) 800, (e) 900, (f) 1000, (g) 1100, (h) 1200, and (i) 1273 K

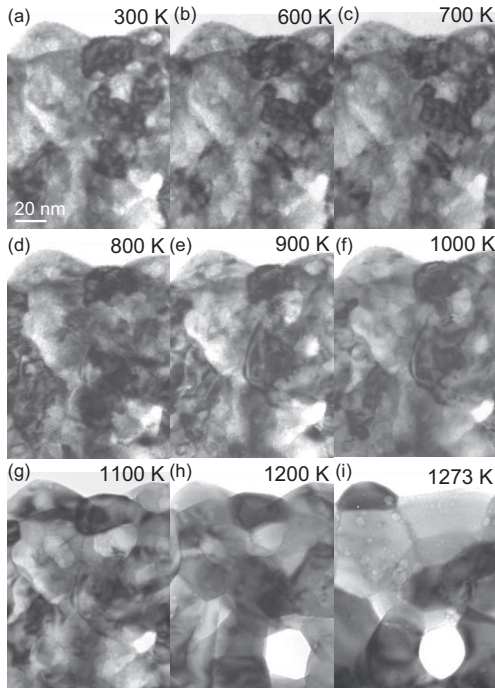


FIG. 10. TEM micrographs shown in Fig. 9 in a larger magnification: (a) before annealing, and after annealing for three minutes at the temperature of (b) 600, (c) 700, (d) 800, (e) 900, (f) 1000, (g) 1100, (h) 1200, and (i) 1273 K.

layer is approximately five times greater on He-W6.

V. SUMMARY AND DISCUSSION

Tungsten was deposited under He plasma environment in this study, and the property of the formed porous He-W co-deposition layer was investigated using TEM observation and TDS analysis. The substrate temperature during the formation of the co-deposition layer was changed from 471-773 K; it was found that the morphology change significantly alters when changing the substrate temperature. At 471 K, the co-deposition layer was comprised of small grains including He bubbles with

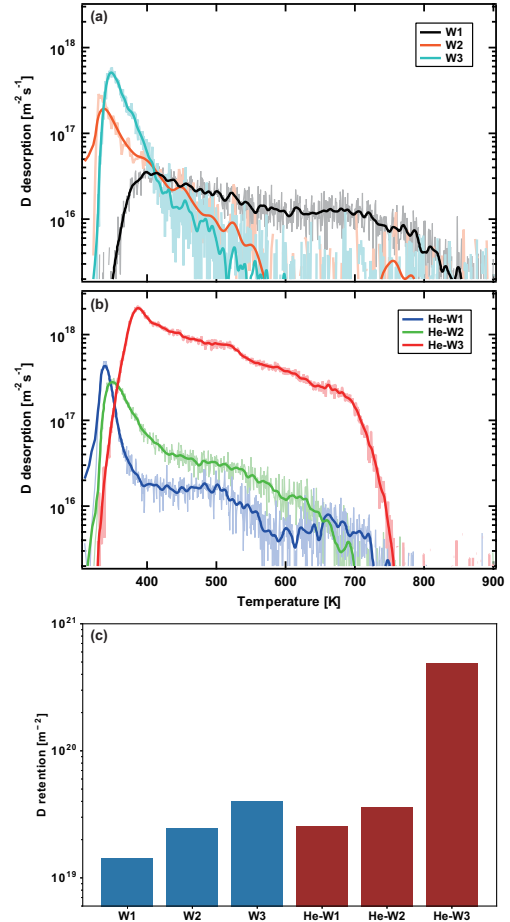


FIG. 11. D desorption rate as a function of the temperature on (a) the samples W1, W2, and W3 and (b) He-W2, He-W4, and He-W6. (c) D retention for the six samples. The ramping rate of the temperature was 0.5 K/s.

crystals of less than 1-2 nm. The sizes of He bubbles and grains increased with the substrate temperature; the size distribution became broader with increasing the temperature and the maximum size was ≈ 100 nm at the substrate temperature of 773 K. We conducted EDS analysis and checked the density of the co-deposition layer.

Tungsten density of the co-deposition layer was always lower than the bulk by 35-40% in average. The density decreases with the depth especially on the co-deposition layer formed at 471 K; the density was less than 40% of the bulk just above the bulk layer. Also, on the co-deposition layer formed at 573 and 773 K, enlarged He bubbles were frequently observed. The results suggested that He density in the co-deposition layer was much greater than the bulk. It is likely that there is a diffusion barrier between the bulk and co-deposition layer, and He atoms tend to accumulate in the co-deposition layer rather than diffused to bulk region.

Small He bubbles with the size of several nm were identified even at the substrate temperature of 471 K; the density of the bubble was much lower than that in the co-deposition layer. No apparent large-sized bubbles (>10 nm) were identified even at the substrate temperature of 773 K, though the size of the bubbles in the co-deposition layer could be ≈ 100 nm. The results suggested that the growth mechanism of He bubbles and voids in the co-deposition layer are quite different from that in the bulk. By conventional He plasma irradiation, such a large He bubbles can only be identified when the surface temperature is higher than ≈ 1000 K, which is the minimum threshold temperature for the fuzz growth [38].

One of the main reasons to cause this difference could be in the fact that the He atoms were trapped in the layer together with W atoms. Because many He atoms hit the surface while the W crystal structures were formed, the He atoms could be captured in a stronger manner in the lattice compared with those penetrated and started to diffuse/migrate in the W matrix. Another factor is the difference in the crystal structure. Although the detailed crystal structure analysis could not be conducted in this study and remains as a future work, diffusion property of He atoms and clusters in the co-deposition layer could be different from that in the bulk. The difference in the diffusion property could lead to the growth rate of He bubbles.

In this study, He desorption was investigated by TDS, and corresponding internal changes were observed on the co-deposition layer formed at 773 K by TEM while the sample was annealed. Compared with the He ion beam case such as in Ref [39], where the ion energy was 5 kV and significant He desorption peaks appeared at 900 K or higher temperatures, one of the differences was in the fact that major He desorption peaks appeared at lower temperature than 900-1000 K. The sample temperature was increased to ~ 1600 K for the TDS analysis; we should note that trapped He was not completely released from the sample and peak would appear in higher temperatures, as was discussed previously [37, 40]. We compared the amount between the samples, though it would be difficult to assess the trapped He atoms quantitatively. It was found that the He retention in the co-deposition layer was much greater than that on bulk material, though the desorption temperature did not alter so much. Focusing on the co-deposition layers, though only one peak ap-

peared below 400-500 K from the co-deposition sample formed at 473 K, the peak became broader on the sample formed at higher temperatures. From the sample formed at 773 K, three peaks were identified: below 600 K, in the range of 700-900 K, and above 1200 K. Below 600 K, He desorption occurred probably from weak trapping sites such as distorted lattice in the vicinity of He bubbles. Around 700-900 K, it was likely that He atoms trapped in bubbles, dislocation, and distortion were released. Helium desorption occurred together with internal structure changes above 1200 K.

Notable difference was in the amount of He retention; the He retention on the co-deposition sample was much greater than that on the bulk. One of the major reasons to cause the enhancement is the thickness of the He containing layer. The thickness of the bubble existing layer was ≈ 50 nm on thin deposited layer sample, while the co-deposition layer had a thickness of ≈ 500 nm, which was an order of magnitude thicker than that in the bulk. The He atoms trapped in the co-deposition layer was not easily released during the He plasma irradiation, or rather they tended to accumulate in the deeper region of the co-deposition layer.

Finally, the He-W co-deposition layer was exposed to deuterium plasma at the surface temperature of 373 K, and the desorption and retention of deuterium were investigated. A good news from the experiments is that almost all D atoms are released from all the prepared substrate at ~ 800 K. Different from He atoms, which exhibited a desorption peak at temperatures higher than 1000 K, D atoms were released easily by heating the temperature around 800 K completely even on the co-deposition surfaces. Desorption from He irradiated samples including co-deposition layer samples had a desorption peak at lower temperature less than 400 K, whereas non-He irradiated sample had a broad desorption in the temperature range of 400-800 K. It was likely that D atoms can be trapped around or together with He bubbles, and those D atoms can be released rather easily. The amount of D retention increased by He plasma irradiation, and the co-deposition sample formed at 773 K has 30 times greater retention than that from the sample without exposure to He plasmas.

As was reviewed by Hammond [41], the relationship between He bubbles and hydrogen retention in tungsten has been thought to be complicated. Some studies suggested that He irradiation decreases the retention of hydrogen isotopes [42, 43], because He bubbles suppress their diffusion as forming a diffusion barrier. On the other hand, others suggested that hydrogen isotope retention increases by He bubbles [44, 45], because He bubbles attract hydrogen isotopes. However, it is likely that the both effects can be understood by treating He bubbles as trapping site for hydrogen; the reduction of the retention could also be caused by trapping hydrogen near the surface due to high He bubble concentrations rather than diffuse to deeper region [41, 46].

In this study, the He plasma irradiation increased the D

retention, especially on the co-deposition layer. This was likely because the co-deposition layer was thick enough and provided sufficient trapping sites for D atoms. The reason that the D retention increased on He irradiated samples in this study could be attributed to the fact that the irradiation temperature of He and D was different. Because the He irradiation was conducted higher temperature than that for D irradiation, the He bubble existing region was deeper, which could lead to form sufficient He bubbles to attract D atoms. Further analysis

of depth profile of D and He densities will be helpful for further understanding of the He roles on D retention.

ACKNOWLEDGMENTS

This work was supported in part by a Grant-in-Aid for Scientific Research 17KK0132, 19H01874 from the Japan Society for the Promotion of Science (JSPS), and the NIFS Collaboration Research program.

-
- [1] D. Nishijima, H. Iwakiri, K. Amano, M. Ye, N. Ohno, K. Tokunaga, N. Yoshida and S. Takamura, *Nucl. Fusion* **45** (2005) 669.
- [2] W. Shu, E. Wakai and T. Yamanishi, *Nucl. Fusion* **47** (2007) 201.
- [3] N. Yoshida, M. Miyamoto, K. Tokunaga, H. Iwakiri, H. Wakimoto, T. Fujiwara and the TRIAM group, *Nucl. Fusion* **43** (2003) 655.
- [4] S. Takamura, N. Ohno, D. Nishijima, and S. Kajita, *Plasma and Fusion Research* **1** (2006) 051.
- [5] S. Kajita, W. Sakaguchi, N. Ohno, N. Yoshida and T. Saeki, *Nucl. Fusion* **49** (2009) 095005.
- [6] M. Baldwin and R. Doerner, *Nucl. Fusion* **48** (2008) 035001 (5pp).
- [7] S. Kajita, N. Ohno, W. Sakaguchi and M. Takagi, *Plasma Fusion Research* **004** (2000) 004.
- [8] S. Kajita, S. Takamura and N. Ohno, *Nucl. Fusion* **49** (2009) 032002.
- [9] T. Petty, M. Baldwin, M. Hasan, R. Doerner and J. Bradley, *Nuclear Fusion* **55** (2015) 093033.
- [10] G. De Temmerman, K. Bystrov, J. J. Zielinski, M. Balden, G. Matern, C. Arnas and L. Marot, *Journal of Vacuum Science & Technology A* **30** (2012) 041306.
- [11] M. Baldwin and R. Doerner, *Journal of Nuclear Materials* **404** (2010) 165.
- [12] S. Takamura, T. Miyamoto, Y. Tomida, T. Minagawa and N. Ohno, *Journal of Nuclear Materials* **415** (2011) S100.
- [13] S. Kajita, N. Ohno, M. Yajima and J. Kato, *Journal of Nuclear Materials* **440** (2013) 55.
- [14] D. Nishijima, M. Baldwin, R. Doerner and J. Yu, *Journal of Nuclear Materials* **415** (2011) S96.
- [15] R. Doerner, M. Baldwin and P. Stangeby, *Nucl. Fusion* **51** (2011) 043001.
- [16] Y. Noiri, S. Kajita and N. Ohno, *Journal of Nuclear Materials* **463** (2015) 285.
- [17] J. Yu, M. Baldwin, R. Doerner, T. Dittmar, A. Hakola, T. Hoschen, J. Likonen, D. Nishijima and H. Toudeshki, *Journal of Nuclear Materials* **463** (2015) 299.
- [18] S. Kajita, S. Kawaguchi, D. Hwangbo, H. Tanaka and N. Ohno, *Plasma Fusion Res.* **13** (2018) 1205001.
- [19] G. D. Temmerman, T. Hirai and R. A. Pitts, *Plasma Physics and Controlled Fusion* **60** (2018) 044018.
- [20] G. D. Temmerman, R. Doerner and R. Pitts, *Nuclear Materials and Energy* **19** (2019) 255.
- [21] K. Woller, D. Whyte and G. Wright, *Nuclear Fusion* **57** (2017) 066005.
- [22] D. Hwangbo, S. Kajita, N. Ohno, P. McCarthy, J. W. Bradley and H. Tanaka, *Nuclear Fusion* **58** (2018) 096022.
- [23] D. Hwangbo, S. Kajita, H. Tanaka and N. Ohno, *Nuclear Materials and Energy* **18** (2019) 250.
- [24] S. Kajita, S. Kawaguchi, N. Ohno and N. Yoshida, *Sci. Rep.* **8** (2018) 56.
- [25] S. Kajita, T. Nojima, T. Okuyama, Y. Yamamoto, N. Yoshida and N. Ohno, *Acta Materialia* **181** (2019) 342.
- [26] K. Schmid, K. Krieger, S. Lisgo, G. Meisl and S. B. and, *Nuclear Fusion* **55** (2015) 053015.
- [27] S. Iyyakkunnel, L. Marot, B. Eren, R. Steiner, L. M. D. Mathys, M. D. P. Chapon and E. Meyer, *ACS Applied Materials & Interfaces* **6** (2014) 11609.
- [28] X. Tang, L. Shi, D. O'Connor and B. King, *Journal of nuclear materials* **446** (2014) 200.
- [29] G. D. Temmerman] and R. Doerner, *Journal of Nuclear Materials* **389** (2009) 479.
- [30] K. Asai, N. Yoshida, N. Ohno, S. Kajita, H. Tanaka, M. Yajima and D. Nagata, *Plasma and Fusion Research* **15** (2020) 1201004.
- [31] S. Kajita, S. Takamura, N. Ohno, D. Nishijima, H. Iwakiri and N. Yoshida, *Nucl. Fusion* **47** (2007) 1358.
- [32] L. Vainshtein, I. Beigman, P. Mertens, S. Brezinsek, A. Pospieszczyk and D. Borodin, *Journal of Physics B, Atomic, Molecular and Optical Physics* **44** (2011) 125201.
- [33] W. Eckstein, IPP (2002) 9/132.
- [34] N. Ohno, Y. Hirahata, M. Yamagiwa, S. Kajita, M. Takagi, N. Yoshida, R. Yoshihara, T. Tokunaga and M. Tokitani, *Journal of Nuclear Materials* **438, Supplement** (2013) S879.
- [35] S. Kajita, N. Yoshida, N. Ohno and Y. Tsuji, *New Journal of Physics* **17** (2015) 043038.
- [36] S. Kajita, A. M. Ito and N. Ohno, *Physics Letters A* **381** (2017) 2355.
- [37] M. Yajima, N. Yoshida, S. Kajita, M. Tokitani, T. Baba and N. Ohno, *Journal of Nuclear Materials* **449** (2014) 9.
- [38] S. Kajita, N. Yoshida, R. Yoshihara, N. Ohno and M. Yamagiwa, *Journal of Nuclear Materials* **418** (2011) 152.
- [39] E. Kornelsen and A. V. Gorkum], *Journal of Nuclear Materials* **92** (1980) 79.
- [40] Y. Gasparyan, V. Efimov and K. Bystrov, *Nuclear Fusion* **56** (2016) 054002.
- [41] K. D. Hammond, *Materials Research Express* **4** (2017) 104002.
- [42] M. Baldwin, R. Doerner, W. Wampler, D. Nishijima, T. Lynch and M. Miyamoto, *Nuclear Fusion* **51** (2011)

- 103021.
- [43] M. Miyamoto, D. Nishijima, Y. Ueda, R. Doerner, H. Kurishita, M. Baldwin, S. Morito, K. Ono and J. Hanna, Nuclear Fusion **49** (2009) 065035 (7pp).
- [44] H. Iwakiri, K. Morishita and N. Yoshida, Journal of Nuclear Materials **307-311** (2002) 135.
- [45] S. Markelj, T. Schwarz-Selinger and A. Založnik, Nuclear Fusion **57** (2017) 064002.
- [46] J. Roth and K. Schmid, Physica Scripta **T145** (2011) 014031.